

Spatially resolved work-function manipulation of azobenzene-functionalized self-assembled monolayers by optical stimulation

Cite as: Appl. Phys. Lett. **124**, 191601 (2024); doi: [10.1063/5.0204610](https://doi.org/10.1063/5.0204610)

Submitted: 22 February 2024 · Accepted: 25 April 2024 ·

Published Online: 7 May 2024



View Online



Export Citation



CrossMark

Jan Böhnke, Beatrice Andres, Larissa Boie, Angela Richter, Cornelius Gahl, Martin Weinelt, ^{a)} and Wibke Bronsch ^{a),b)}

AFFILIATIONS

Freie Universität Berlin, Fachbereich Physik, Arnimallee 14, 14195 Berlin, Germany

^{a)} Authors to whom correspondence should be addressed: weinelt@physik.fu-berlin.de and wibke.bronsch@fu-berlin.de

^{b)} Present address: Elettra-Sincrotrone Trieste S.C.p.A., Strada Statale 14-km 163.5 in AREA Science Park, 34149 Basovizza, Trieste, Italy.

ABSTRACT

Strongly differing static dipole moments of the *trans* and *cis* isomers of photochromic azobenzene allow for optical switching of the work function of azobenzene-functionalized self-assembled monolayers (SAMs). We apply these properties in a fundamental experiment to manipulate the area size of the switched SAM. Azobenzene molecules were excited by ultraviolet laser illumination, and the transient isomerization profile of the SAM was spatially resolved recording photoemission electron microscopy images. Thereby, we demonstrate the spatial tuning of the SAM's work function and discuss the role of the laser spot profile in generating sharp edges or gradual changes of the work function.

© 2024 Author(s). All article content, except where otherwise noted, is licensed under a Creative Commons Attribution (CC BY) license (<https://creativecommons.org/licenses/by/4.0/>). <https://doi.org/10.1063/5.0204610>

Azobenzene-based self-assembled monolayers (SAMs) are prototype systems for photoresponsive surfaces.^{1–7} Their photochromic switching ability can, e.g., be used to tune level alignments at interfaces.^{4–7} Here, we discuss local changes of the SAM's work function induced by altering the static dipole moment of the chromophores with controlled photoisomerization. Azobenzene is a conformational switch, consisting of two phenyl rings coupled via a dinitrogen bond (see inset in Fig. 1). In its *trans* form, the molecule is planar and the two rings are on opposite sides of the dinitrogen bond axis. In the *cis* conformation, both rings are on the same side of the reference plane. Therefore, the molecule has no static dipole moment in the *trans* configuration but is strongly polar in its *cis* state.⁸ Dissolved in solution, light in the blue to ultraviolet (UV) range triggers photoswitching between the two isomers.⁹ For fabricating photoresponsive surfaces, we linked azobenzene to Au(111)/Mica substrates via an alkanethiol chain following an elaborated procedure.^{10–14} Utilizing a linker with a chain length of 11 carbon atoms, the azobenzene head groups are sufficiently decoupled from the surface (see Fig. 1 insets). We will denominate the azobenzene derivative 11-(4-(phenyldiazenyl)phenoxy)-undecane-1-thiol used in this work as Az11. It is essential to dilute the chromophore density to prevent steric hindrance.^{12,15} We observed efficient photoswitching in mixed SAMs of Az11 and a pure

alkanethiolate of comparable length (C12) prepared in a wet-chemical process.¹³ In this work, we used samples with 50% Az11 surface coverage.¹³

Near edge x-ray absorption fine structure (NEXAFS) spectroscopy showed that in a pure Az11 SAM the *trans* chromophores are tilted by about 30° from the surface plane.¹² In diluted SAMs, the chromophores tilt further toward the SAM surface.¹⁴ When switching into its *cis* form, the molecule flips the upper phenyl ring and the *z*-component of its static dipole moment points toward the surface. Thus, the work function of the SAM/Au(111) sample increases with the number of molecules in *cis* configuration.^{4,7,16} This allows us to locally tune the work function and image areas of switched molecules in the SAM via spatially resolved photoelectron emission. Although external work function manipulations of azobenzene-functionalized surfaces have been studied by several groups,^{4–7,17–20} so far no analysis of the switched area was performed. Controlling homogeneity and locality of the switched area is highly relevant for future applications. Here, we use the photoemission electron microscopy (PEEM) mode of a time-of-flight momentum microscope for getting access to spatial modulations in the micrometer range. PEEM allows us to analyze the size and profile of switched areas. We demonstrate that the absolute value of the local work function and hence the isomerization profile as

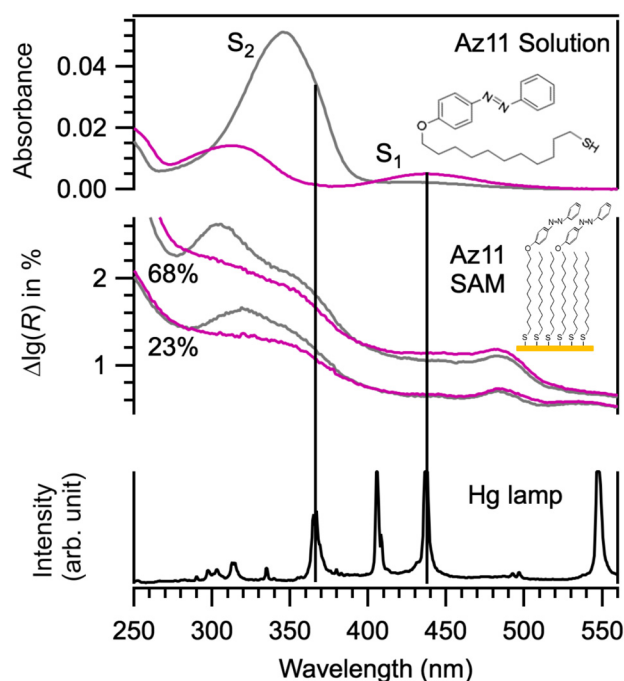


FIG. 1. Comparison of the mercury lamp emission lines and the absorbance of Az11. Top: Absorbance of non-interacting *trans* (grey curve) and *cis* (magenta curve) Az11 molecules in solution. Inset: Structural formula of Az11 in *trans* configuration. Middle: Differential-reflectance signal of a 23% and 68% Az11-SAM in an all-*trans* configuration (grey curves) and under 365 nm illumination (magenta curves) as published in Moldt *et al.*¹³ Inset: Cartoon of the Az11-SAM in *trans* configuration diluted with C12 spacer-molecules. Bottom: emission spectrum of the mercury lamp. Vertical lines indicate the most relevant emission lines of the Hg lamp in relation to the absorption bands of non-interacting and excitonically coupled Az11 molecules.

well as the time span to switch the work function can be tuned by laser illumination.

In Fig. 1, we compare the absorbance of Az11 molecules in the methanol solution and the differential reflectance of mixed SAMs from Ref. 13 with the spectrum of a mercury arc lamp. In the SAM, the S_2 band splits and its maximum shifts to higher energies with increasing Az11 percentage (Fig. 1, middle panel). This is attributed to excitonic coupling between the *trans* isomers, whereby the $\pi\pi^*$ transition-dipole moments form an H-aggregate. Molecules switched to the *cis* state show no excitonic coupling.²¹ Irradiation at the low-energy edge of the S_2 absorption band at about 370 nm leads to *trans-cis* isomerization in the SAM. The *cis-trans* back-isomerization is triggered by illumination either at the high energy edge of the S_2 band or in the S_1 band, showing up at around 440 nm.²¹

We mainly used two complementary photon sources, a continuous wave (cw) laser (372 nm) and a Hg lamp for illumination in the S_2 and S_1 absorption bands, respectively. Simultaneous excitation facilitates optical tuning of the *cis-trans* ratio at the functionalized surface. The cw laser initiates the *trans-cis* isomerization only, whereas the Hg lamp contributes to both *trans-cis* and *cis-trans* configuration changes. As illustrated in Fig. 1, several emission lines of the mercury lamp are in the range of the S_1 and S_2 absorption bands of the Az11 SAM.

The intense emission line at 436 nm illuminates in the S_1 band center, leading to efficient *cis-trans* isomerization. The emission line at 365 nm instead triggers *trans-cis* switching. Considering the relative photon flux of both emission lines we estimated the photostationary state (PSS) of the mercury lamp (Hg-PSS) as discussed in detail in the supplementary material (supplementary material, Sec. II). We find photon fluxes of $j_{436\text{nm}} = 1.9 \times 10^{14} \text{ cm}^{-2}$ and $j_{365\text{nm}} = 3.3 \times 10^{14} \text{ cm}^{-2}$ leading to a PSS with 67% *cis* molecules. Starting from this PSS, a maximal work function change of 30 meV can be reached when tuning toward a pure *cis* SAM by simultaneous laser illumination at 372 nm.²¹

The high-energetic lines of the mercury lamp lead to photoelectron emission from the functionalized surface.^{16,21} We perform spatially resolved photoemission experiments in an ultra-high vacuum chamber using a momentum microscope.^{22,23} The instrument has been set up in collaboration with Schönense. In this work, we use the instrument's spatially resolving "Gaussian" imaging mode comparable to a photoelectron emission microscope.²² The field of view (FoV) on the sample surface is selected by real space apertures inserted between two zoom optics. Photoelectrons are detected after a time-of-flight tube by single event counting through a delay line detector.²⁴ A $(5 \times 5) \text{ mm}^2$ chess-patterned gold-on-silicon sample (Chessy, Plano) was characterized for initial alignment and calibration of the focusing and magnifying electron optics, exploiting the instrumental resolution. Figure 2 shows spatially resolved electron images of the $(10 \times 10) \mu\text{m}^2$ chess patterns. With a FoV of 100 and 800 μm diameter, we obtained spatial resolutions below 3 and 16 μm , respectively (see the supplementary material,

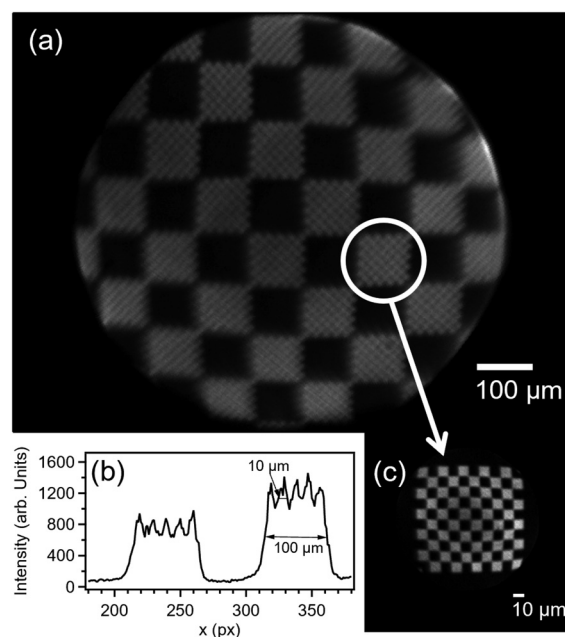


FIG. 2. (a) Spatially resolved photoelectron emission of a Chessy sample for calibration of the focusing and magnifying electron optics. We selected a PEEM FoV with a diameter of 800 μm to spatially resolve the work function changes. The line profile in x direction in (b) indicates the ability to resolve 10 μm squares with this setting. Inset (c) shows an image with a FoV of 100 μm diameter and a spatial resolution below 3 μm taken with a different lens magnification setting (see the supplementary material, Sec. V).

Sec. V). Since the measurements on the Az11 SAMs required a large FoV, we used the latter settings which still provide appropriate spatial resolution.

Trans-cis isomerization of the SAM in a selected area was triggered focusing the 372 nm laser beam onto the sample. An image of the laser spot recorded with a CCD camera is shown in Fig. 3(a) together with horizontal (x) and vertical (y) beam profiles taken across the spot center. The focus has an elliptical profile with full width at half maximum (FWHM) of 19 and $25 \pm 1 \mu\text{m}$. Beam profiles were modeled using 2D Gaussian and Cauchy distributions. The latter accounts particularly better for the projection of the laser spot along the direction of incidence x .

To spatially resolve the work function shift across the sample, we recorded local electron yield (LEY) images in PEEM mode with and without laser illumination. The 372 nm beam was focused in the upper left part of the FoV and impinged at a grazing angle of 22° onto the sample. This expands the horizontal spot profile to a FWHM of around $67 \mu\text{m}$. Figures 3(b) and 3(c) show the detector sensitivity corrected normalized images $[\text{LEY}(\text{Hg} + 372) - \text{LEY}(\text{Hg})]/\text{LEY}(\text{Hg}) = (\Delta\text{LEY}/\text{LEY}_0)$ for identical spot profiles, but changing laser power by one order of magnitude. Before image acquisition, the sample was exposed to laser illumination for about 300 s while the acquisition time for each images was about 150 s. The PEEM image in Fig. 3(b) was recorded with a laser power of $1.7 \pm 0.3 \mu\text{W}$. This corresponds to a photon flux of $\sim 1 \times 10^{17} \text{ cm}^{-2} \text{ s}^{-1}$ in the laser spot center, leading to about 1 switching event every 10 s.^{13,21} At this threshold fluence, we start to observe a local shift of the PSS state toward higher work function (higher density of *cis*-isomers). From the horizontal and vertical profiles, we estimate a spot size of $60 \times 200 \mu\text{m}^2$, about 3–4 times larger than the FWHM of the laser focus.

Increasing the 372 nm photon flux by a factor of 10, the area in Fig. 3(c) showing a decreased EY is more pronounced and significantly

larger. Horizontal and vertical profiles reveal a magnification of the projected laser focus FWHM by a factor of 10. While the differential photoemission intensity ΔLEY changes gradually along the direction of laser incidence x , comparably sharp edges and a nearly flat top are observed along the y -direction.

Taking into account the laser-focus profile, we modeled the expected local work function shifts $\Delta\Phi$ assuming first-order kinetics according to

$$\Delta\Phi(\vec{j}) = \Delta\Phi_{\text{PSS}} \frac{\tilde{r}}{j + \tilde{r}}. \quad (1)$$

For a detailed derivation of this equation, we refer to Ref. 21. Here, $\tilde{j} = j(436 \text{ nm})/j(372 \text{ nm})$ corresponds to the photon flux ratio of Hg lamp and 372 nm laser, while $\tilde{r} = \tilde{\sigma}(372 \text{ nm})/\tilde{\sigma}(436 \text{ nm})$ corresponds to the ratio of effective isomerization cross sections for both light sources. $\Delta\Phi_{\text{PSS}}$ denotes the work function difference between the PSSs reached under 372 and 436 nm illumination only. From the wavelength dependence of the effective isomerization cross section across the S_2 absorption band, we obtain $\tilde{\sigma}(372 \text{ nm}) \approx \tilde{\sigma}(365 \pm 5 \text{ nm}) = 1.4 \times 10^{-18} \text{ cm}^2$.^{13,21} In the case of the S_1 band, we approximate $\tilde{\sigma}(436 \text{ nm})$ by $\tilde{\sigma}(455 \text{ nm}) = 1.2 \times 10^{-18} \text{ cm}^2$, which is known from NEXAFS experiments on Az11 SAMs.¹³ For our simulations, we assumed homogeneous illumination by the Hg lamp in the PEEM's FoV and fitted the measured profile of the laser spot with either Cauchy or Gaussian distributions (see the supplementary material, Sec. I). Elliptical profiles account for the different widths in horizontal and vertical directions. Figures 4(a) and 4(b) show calculated local work function changes for laser intensities of 1.7 and $17 \mu\text{W}$, respectively. The color scale ranges from the PSS of the Hg lamp [$\Phi(\text{Hg})$, white] to the maximal work function change reached upon 372 nm illumination only [$\Phi(372)$, red], i.e., the PSS with predominantly *cis* Az11 chromophores. As expected, the Cauchy distribution gives

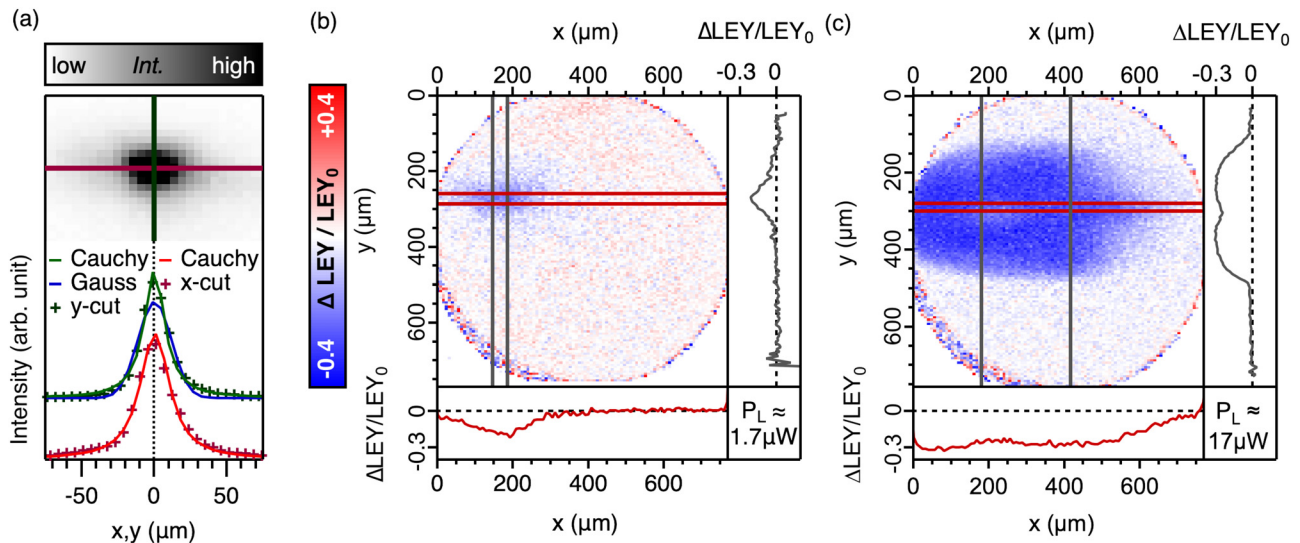


FIG. 3. (a) CCD image of the cw laser spot. Vertical and horizontal cuts through the spot profile indicate contributions with a Lorentzian-like tail (Cauchy distribution). (b) and (c) Normalized PEEM images $[\text{LEY}(\text{Hg} + 372) - \text{LEY}(\text{Hg})]/\text{LEY}(\text{Hg})$ recorded for a laser power P_L of 1.7 and $17 \mu\text{W}$, respectively. The images show a decrease in the local electron yield (LEY) in the areas where the laser spot was positioned. Side panels show profiles in vertical and horizontal directions extracted in the range indicated by horizontal (grey) and vertical (red) lines.

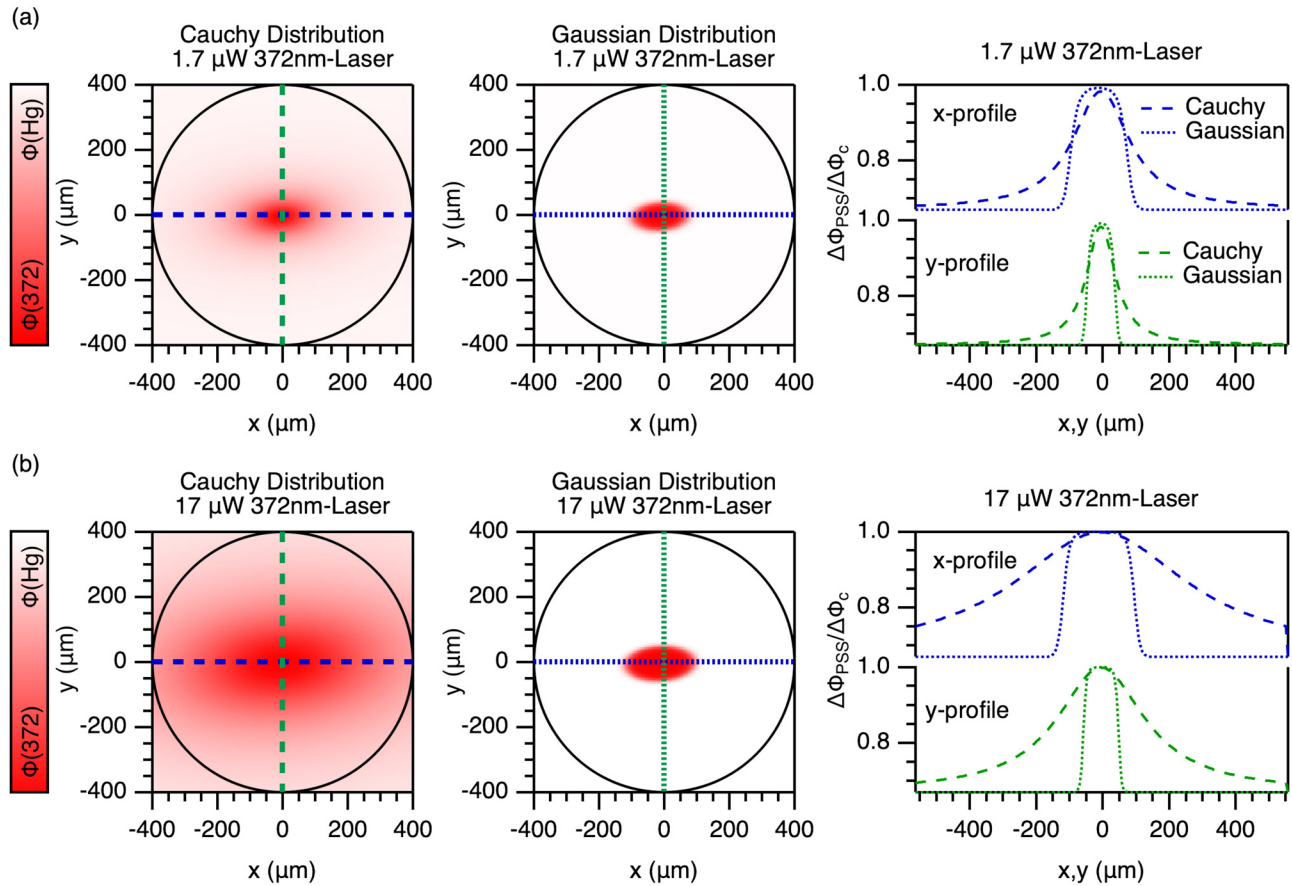


FIG. 4. (a) and (b) Modeling of the work function change based on 2D fits of the 372 nm laser beam-profile using Cauchy and Gaussian distributions (left and middle panels). The modeling of the PEEM data was performed based on Eq. (1) applied for every pixel for $P_L = 1.7$ (a) and $17 \mu\text{W}$ (b), respectively. In the left panels, we compare the vertical and horizontal profiles for Cauchy (dashed) and Gaussian (dotted) distributions. Note that changes in LEY and work function are proportional (see the supplementary material, Sec. III).

smooth changes of the work function over several hundreds of micrometer away from the spot center at $(0, 0)$. In contrast, for a Gaussian distribution, we observe work function profiles with steepened edges and a flat top. None of the models perfectly describes the measured laser spot, but a combination of both contains all characteristics of the switched area. The shape of the beam profile is, thus, essential for the work function gradient from the center of the switched spot to the non-changed environment, whereas the local photon flux ratio of the laser beam and the Hg lamp determines the magnitude of the local work function shift. The tails of the Cauchy profile $\propto 1/x^2$ lead to an extended switched area, those of a Gaussian $\propto \exp(-x^2)$ to steepened edges and a pronounced flat top along the y -direction. An increase in the local work function $\Delta\Phi$ upon *trans-cis* isomerization leads to a decrease in the local electron yield ΔLEY . In Sec. III of the supplementary material, we demonstrate $\Delta\Phi \propto -\Delta\text{LEY}$. Thus, simulated patterns of $\Delta\Phi$ and measured ΔLEY profiles are quantitatively comparable. Comparing the simulations (cf. Fig. 4) with our data (cf. Fig. 3), we conclude that only those areas hit by the laser beam are switched. In the PEEM experiment, we spatially resolve the photoelectron yield and not directly the work function.

The photon flux in the laser spot not only varies the local PSS but also the kinetics to reach this PSS. As a measure for the overall switching kinetics, we evaluate the transient of the total electron yield $\text{TEY}(t)$ by summing up the electron count-rate in the complete FoV as a function of exposure time t . As shown in Fig. 5(a), $\text{TEY}(t)$ decreases as soon as the laser beam illuminates the sample, since the Az11 SAM changes toward the new PSS that includes overall a higher fraction of *cis* isomers.^{4,16,21} When turning laser illumination off, the ensemble of Az11 molecules relaxes back to the Hg-PSS.

To describe the transient work function shift $\Delta\Phi(t)$, which expresses the ensemble switching kinetics, the time-dependent change in the local fraction of *cis* molecules $\Delta\chi_c(t)$ has to be considered (for details, see the supplementary material, Sec. IV):

$$\Delta\Phi(x, y, t) = \Delta\Phi_{\text{PSS}} \cdot \Delta\chi_c(x, y, t) \quad (2)$$

with

$$\begin{aligned} \Delta\chi_c(x, y, t) &= \chi_c(x, y, t) - \chi_c(0) \\ &= \Delta\chi_{c,\text{PSS}}(x, y) \cdot (1 - e^{-t \cdot (j_1(x,y) \cdot \vec{\sigma}_1 + j_2 \cdot \vec{\sigma}_2)}) \end{aligned}$$

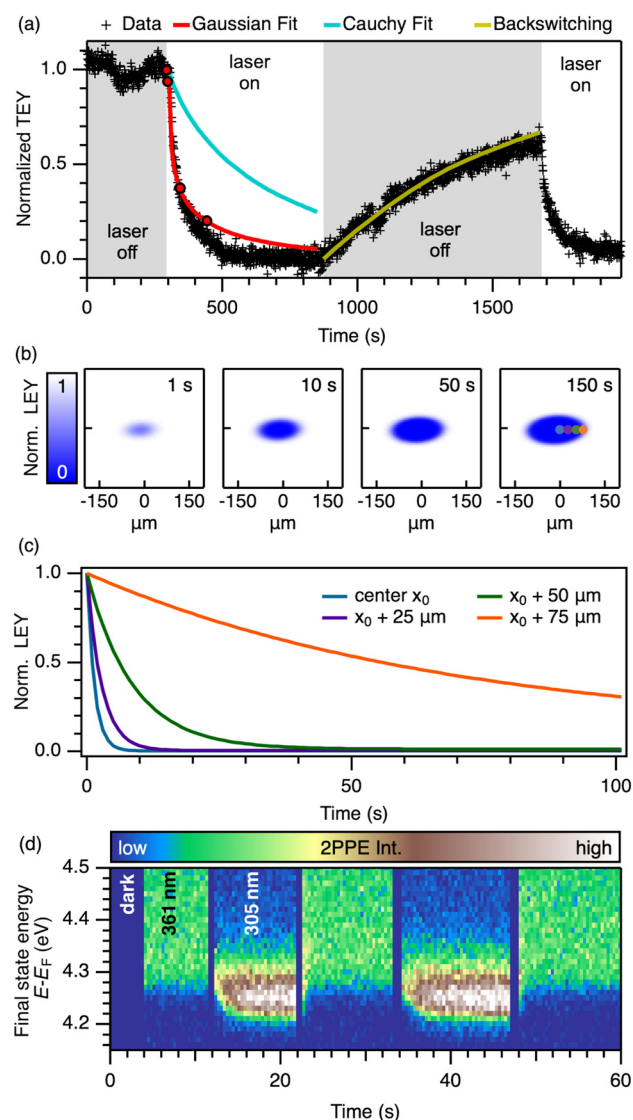


FIG. 5. (a) Temporal evolution of the total electron yield (TEY) integrated over a FoV with a diameter of $800\ \mu\text{m}$ after turning on and off the cw laser with $48\ \mu\text{W}$ incident power. We compare the acquired data (black markers) with the modeled curves for Gaussian (red curve) and Cauchy (cyan curve) shaped beam profiles. The yellow-green curve shows the expected behavior for switching back after turning off the laser. (b) Modeled spatial distribution of the LEY across the sample at 1, 10, 50, and 150 s [cf. red markers in panel (a)] after having turned on the laser with $48\ \mu\text{W}$ incident power. Norm. LEY = 1 corresponds to the LEY at Hg-PSS and 0 to the LEY at the 372 nm-PSS. (c) Local switching kinetics curves colored corresponding to the markers in panel b indicating their spatial positions: central position x_0 of the spot profile (blue), $25\ \mu\text{m}$ (violet), $50\ \mu\text{m}$ (green), and $75\ \mu\text{m}$ (orange) away from the spot center. (d) Single wavelength 2PPE measurements as a function of illumination time resolve the switching kinetics directly monitoring the work function change.

with $\Delta\chi_{c,\text{PSS}}(x,y) = \chi_c(x,y,\infty) - \chi_c(0)$, $j_{1,2} = j(372\ \text{nm})$, $j(436\ \text{nm})$, and $\tilde{\sigma}_{1,2} = \tilde{\sigma}(372\ \text{nm})$, $\tilde{\sigma}(436\ \text{nm})$.

The solid lines in Fig. 5(a) show the calculated change of the TEY for the fitted Cauchy and Gaussian laser spot profiles (cf. Fig. 3). Using

the Cauchy distribution, we get poor agreement between modeled and measured switching kinetics (cyan line). The Gaussian beam profile (red line) shows a much better agreement. This matches the observation of sharp edges of the switched areas, shown by the line profiles in Fig. 3(c). We modeled the temporal evolution of the spatial work function distribution in a defined FoV to illustrate how the LEY gradually evolves under laser illumination. Figure 5(b) shows exemplary images after 1, 10, 50, and 150 s laser illumination with a Gaussian profile, Fig. 5(c), the corresponding kinetics curves for selected positions in real space. In the center of the beam, the PSS state is close to a pure *cis* SAM and is reached after few seconds for $48\ \mu\text{W}$ laser power (blue curve). In the tails of the laser spot, the local PSS is not reached within 100 s (orange curve). The fast and precise work function tuning modeled for the spot center can be shown using photoemission from a pulsed laser source operated at a wavelength in the S_2 band. This gives excitation densities high enough to induce two-photon photoemission (2PPE) and enables direct tracing of the work function change as shown in Fig. 5(d) for 361 and 305 nm photons. Upon excitation with 305 nm, the low energy cutoff of the photoemitted electron spectrum shifts toward 4.22 eV with respect to 4.27 eV when illuminated by 361 nm. This indicates a work function shift of 50 meV. Enhancing the capabilities of the experimental PEEM setup with a new pulsed laser source (supplementary material, Sec. V) will enable spatially resolved measurements of the work function distribution, paving the path for transient μm work function patterning beyond the LEY signatures.

In conclusion, we showed that well-defined and homogeneous switched areas can be produced by illuminating an azobenzene-functionalized surface with a focused UV beam without the need of current patterning techniques with predefined vignettes,^{25,26} enabling on-the-fly modifications. When shaping the beam profile, the absolute value of the local work function as well as the timescale required to switch the work function can be controlled. The switched area and isomerization profile depend on the laser spot profile paving the route toward designing cheap organic optoelectronic devices with an active area, tuning not only the work function, but, e.g., the lateral excitonic coupling among the photoswitches.

See the supplementary material for details on the 2D spot profile modeling, the determination of the mercury discharge lamp induced photostationary state, and the conversion of the work function changes into a photoelectron yield. These input parameters were used for simulating the spatially resolved work function changes of the diluted Az11 SAM. Furthermore, we show the characterization of the PEEMs spatial resolution and the extraction procedure for obtaining the difference PEEM images shown in the main text.

We thank Rafal Klajn for the kind supply of the Az11 molecules and Johannes Mosig for fruitful discussions and computational support. J.B. thanks the International Max Planck Research School for Elementary Processes in Physical Chemistry for the financial support in the initial phase of his Ph.D. This project was supported by Deutsche Forschungsgemeinschaft via the Collaborative Research Center TRR 227 on Ultrafast Spin Dynamics, projects A01 and B07. Part of the equipment was financed by the Deutsche Forschungsgemeinschaft via the program for major research instrumentation (91b GG).

AUTHOR DECLARATIONS

Conflict of Interest

The authors have no conflicts to disclose.

Author Contributions

Jan Böhnke: Data curation (lead); Formal analysis (equal); Investigation (equal); Validation (equal); Visualization (equal); Writing – original draft (equal); Writing – review & editing (equal). **Beatrice Andres:** Conceptualization (equal); Data curation (equal); Investigation (lead); Supervision (equal); Writing – review & editing (equal). **Larissa Boie:** Investigation (equal); Writing – review & editing (equal). **Angela Richter:** Data curation (equal); Investigation (equal); Writing – review & editing (equal). **Cornelius Gahl:** Conceptualization (equal); Investigation (equal); Methodology (equal); Writing – review & editing (equal). **Martin G. Weinelt:** Conceptualization (equal); Funding acquisition (lead); Project administration (lead); Resources (lead); Supervision (equal); Writing – original draft (equal); Writing – review & editing (equal). **Wibke Bronsch:** Conceptualization (equal); Data curation (equal); Formal analysis (lead); Investigation (equal); Methodology (lead); Supervision (equal); Validation (equal); Visualization (lead); Writing – original draft (lead); Writing – review & editing (lead).

DATA AVAILABILITY

The data that support the findings of this study are available from the corresponding authors upon reasonable request.

REFERENCES

- J. D. Steen, D. R. Duijnste, and W. R. Browne, *Surf. Sci. Rep.* **78**, 100596 (2023).
- K. Ichimura, S.-K. Oh, and M. Nakagawa, *Science* **288**, 1624 (2000).
- N. Crivillers, E. Orgiu, F. Reinders, M. Mayor, and P. Samori, *Adv. Mater.* **23**, 1447 (2011).
- L. F. N. Ah Qune, H. Akiyama, T. Nagahiro, K. Tamada, and A. T. S. Wee, *Appl. Phys. Lett.* **93**, 083109 (2008).
- N. Crivillers, A. Liscio, F. Di Stasio, C. Van Dyck, S. Osella, D. Cornil, S. Mian, G. M. Lazzarini, O. Fenwick, E. Orgiu, F. Reinders, S. Braun, M. Fahlman, M. Mayor, J. Cornil, V. Palermo, F. Cacialli, and P. Samori, *Phys. Chem. Chem. Phys.* **13**, 14302 (2011).
- N. Crivillers, S. Osella, C. Van Dyck, G. M. Lazzarini, D. Cornil, A. Liscio, F. Di Stasio, S. Mian, O. Fenwick, F. Reinders, M. Neuburger, E. Treossi, M. Mayor, V. Palermo, F. Cacialli, J. Cornil, and P. Samori, *Adv. Mater.* **25**, 432 (2013).
- T. Nagahiro, H. Akiyama, M. Hara, and K. Tamada, *J. Electron Spectrosc. Relat. Phenom.* **172**, 128 (2009).
- G. S. Hartley and R. J. W. Le Fevre, *J. Chem. Soc.* 531 (1939).
- H. M. D. Bandara and S. C. Burdette, *Chem. Soc. Rev.* **41**, 1809 (2012).
- W. Freyer, D. Brete, R. Schmidt, C. Gahl, R. Carley, and M. Weinelt, *J. Photochem. Photobiol., A* **204**, 102 (2009).
- R. Klajn, *Pure Appl. Chem.* **82**, 2247 (2010).
- C. Gahl, R. Schmidt, D. Brete, E. R. McNellis, W. Freyer, R. Carley, K. Reuter, and M. Weinelt, *J. Am. Chem. Soc.* **132**, 1831 (2010).
- T. Moldt, D. Brete, D. Przyrembel, S. Das, J. R. Goldman, P. K. Kundu, C. Gahl, R. Klajn, and M. Weinelt, *Langmuir* **31**, 1048 (2015).
- T. Moldt, D. Przyrembel, M. Schulze, W. Bronsch, L. Boie, D. Brete, C. Gahl, R. Klajn, P. Tegeder, and M. Weinelt, *Langmuir* **32**, 10795 (2016).
- N. Heinemann, J. Grunau, T. Leifßner, O. Andreyev, S. Kuhn, U. Jung, D. Zargarani, R. Herges, O. Magnussen, and M. Bauer, *Chem. Phys.* **402**, 22 (2012).
- W. Bronsch, D. Przyrembel, L. Boie, C. Gahl, and M. Weinelt, *Appl. Phys. Lett.* **111**, 081601 (2017).
- B. Stiller, G. Knochenhauer, E. Markava, D. Gustina, I. Muzikante, P. Karageorgiev, and L. Brehmer, *Mater. Sci. Eng.* **8–9**, 385 (1999).
- D. Gustina, E. Markava, I. Muzikante, B. Stiller, and L. Brehmer, *Adv. Mater. Opt. Electron.* **9**, 245 (1999).
- S. Schuster, M. Fuser, A. Asyuda, P. Cyganik, A. Terfort, and M. Zharnikov, *Phys. Chem. Chem. Phys.* **21**, 9098 (2019).
- S. Osella, D. Cornil, and J. Cornil, *Phys. Chem. Chem. Phys.* **16**, 2866 (2014).
- W. Bronsch, T. Moldt, L. Boie, C. Gahl, and M. Weinelt, *J. Phys.: Condens. Matter* **29**, 484002 (2017).
- G. Schönhense, K. Medjanik, and H.-J. Elmers, *J. Electron Spectrosc. Relat. Phenom.* **200**, 94 (2015).
- G. Schönhense and H.-J. Elmers, *J. Vac. Sci. Technol., A* **40**, 020802 (2022).
- A. Oelsner, M. Rohmer, C. Schneider, D. Bayer, G. Schönhense, and M. Aeschlimann, *J. Electron Spectrosc. Relat. Phenom.* **178–179**, 317 (2010).
- Y. Yue, R. Azumi, and Y. Norikane, *ChemPhotoChem* **4**, 5383 (2020).
- S. Bakker, E. de Korver, M. Fransen, E. Kamer, G. A. Metselaar, A. C. C. Esteves, and A. P. H. J. Schenning, *ACS Appl. Opt. Mater.* **1**, 403 (2023).